ACS APPLIED MATERIALS & INTERFACES

www.acsami.org

Forum Article

Enhanced Elastocaloric Effects in γ-Graphyne

Guilherme B. Kanegae, Marcelo L. Pereira Junior, Douglas S. Galvão, Luiz A. Ribeiro Junior, and Alexandre F. Fonseca*

Cite This: ACS Appl. Mater. Interfaces 2025, 17, 13074−13082

Read Online

ACCESS | Metrics & More | Article Recommendations | Supporting Information

ABSTRACT: The global emphasis on sustainable technologies has become a paramount concern for nations worldwide. Specifically, numerous sustainable methods are being explored as promising alternatives to the well-established vapor-compression technologies in cooling and heating devices. One such avenue gaining traction within the scientific community is the elastocaloric (eC) effect. This phenomenon holds promise for efficient cooling and heating processes without causing environmental harm. Studies carried out at the nanoscale have demonstrated the efficiency of the eC effect, proving to be comparable to that of state-of-the-art macroscopic systems. In this study, we used classical molecular dynamics simulations to investigate the elastocaloric effect for the recently synthesized γ-graphyne. Our analysis goes beyond obtaining changes in eC temperature and the coefficient of performance (COP) for two species of γ-graphyne nanoribbons (armchair and zigzag). We also explore their dependence on various conditions, including whether they are deposited on a substrate or prestrained. Our findings reveal a substantial enhancement in the elastocaloric effect for γ-graphyne nanoribbons when subjected to prestrain, amplifying it by at least 1 order of magnitude. Under certain conditions, the changes in the eC temperature and the COP of the structures reach expressive values as high as 224 K and 14, respectively. We discuss the implications of these results by examining the shape and behavior of the carbon−carbon bond lengths within the structures.

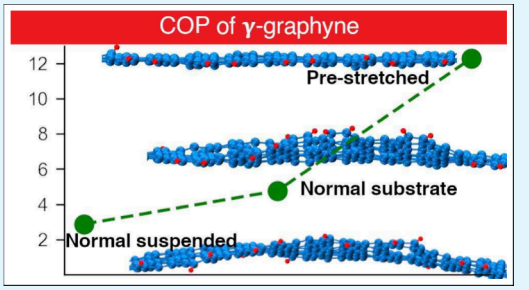

KEYWORDS: *Graphyne, Elastocaloric effect, Nanoribbons, Molecular Dynamics, Prestraining*

1. INTRODUCTION

Growing concerns about climate change and the push for sustainable development of nations are steering scientific and technological research.[1] Addressing the escalating global demand for cooling while mitigating greenhouse gas emissions presents a significant challenge for materials scientists and engineers.[2] Understanding material properties is crucial for technological progress toward these efforts. It may provide the most direct route to meeting these diverse demands.

In recent decades, the unique properties of nanomaterials (such as graphene) have been widely exploited, playing a fundamental role in advancing several new technologies across various domains.[3] Despite concerns about potential environmental hazards associated with nanomaterials (such as nanoparticles),[4] the literature emphasizes the substantial benefits of nanotechnology in critical areas crucial for sustainable human development.[5]

A key concern in sustainability is the development of environmentally friendly cooling devices.[6] Material scientists are exploring alternatives to the conventional vapor-compression cooling technology, leading to the emergence of solid-state refrigeration.[7,8] Based on the caloric effect, this approach involves generating or absorbing heat in response to an external field, which can be electrical, magnetic, or mechanical.[9,10] In the mechanical category, barocaloric (bC)[11,12] and elastocaloric (eC)[13,14] effects are prominent, allowing a system to change its temperature through hydrostatic and stress deformations, respectively. Importantly, efficient elastocaloric materials include natural rubber,[11,14] Ni−Ti,[15] and Cu−Zn−Al shape memory alloys,[16] among others.[17] Developing solid-state refrigeration also offers a distinct advantage, such as miniaturization.[18,19]

While computational studies on the eC effect in nanomaterials are still in their early stages, noteworthy findings have already been obtained.[20−27] Lisenkov et al.[20] pioneered molecular dynamics-based predictions for eC effects in graphene and carbon nanotubes. Similarly, Zhang[21] explored eC effects in boron-nitride nanotubes, and Patel and Kumar[22] predicted the eC effect in zinc-oxide nanowires.

Regarding the methodological aspects of the eC effect, Cantuario and Fonseca[23] introduced a novel protocol to simulate complete thermodynamic cycles of refrigeration. Their work estimated the coefficient of performance (COP) of carbon nanotubes as solid nanorefrigerants, demonstrating

Special Issue: Forum Focused on South American Authors

Received: February 27, 2024
Revised: April 23, 2024
Accepted: April 26, 2024
Published: May 6, 2024

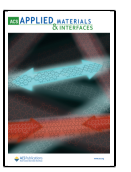

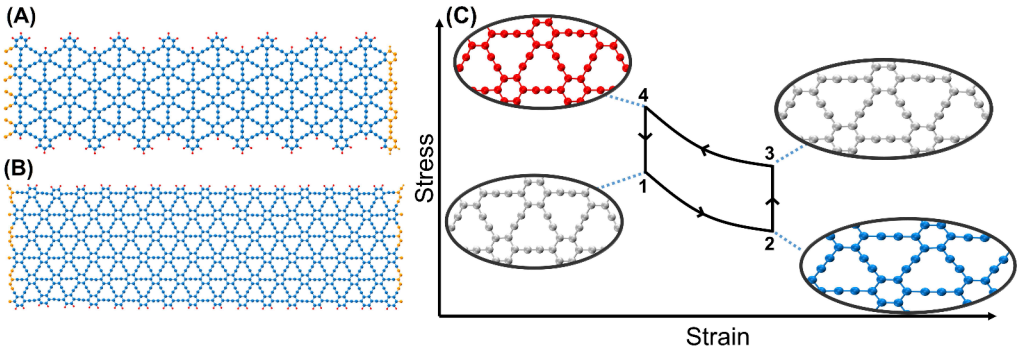

Figure 1. Zigzag (A) and armchair (B) γ-graphyne nanoribbons. Free/movable carbon and hydrogen atoms are indicated in blue and red colors, respectively. Orange indicates the atoms that are either fixed or rigidly moved in the finite-length simulations. Panel (C) shows the stress−strain thermodynamic cycle, with insets depicting thermodynamic equilibrium states. White, red, and blue colors correspond to temperatures equal to, greater than, and smaller than the operator temperature.

comparable or superior efficiency to current vapor-compression refrigerators. In addition, Silva and Fonseca[24] extended these calculations to determine the COP of different carbon nanotubes across a broad range of operating temperatures. A similar method was applied to unveil eC behaviors in graphene kirigami.[25] Utilizing different protocols, Zhao, Guo, and Zhang[26] and Cai, Yang, and Akbarzadeh[27] predicted significant COP in 3D graphene architectures and graphene origami, respectively. However, to our knowledge, the eC effect in graphyne-based structures remains to be fully explored.

In 1987, Baughman, Eckhardt, and Kertesz introduced porous two-dimensional carbon phases known as *graphynes*, proposing structures formed by replacing carbon−carbon bonds in a graphene hexagonal network with acetylene chains —C≡C—$_n$.[28] For $n > 1$, these structures are termed graph*di*yne ($n = 2$), graph*tri*yne ($n = 3$), etc. Like graphene, graphynes are one-atom thick and predicted to exhibit high carrier mobility[29] and robust mechanical strength.[30] Differently, graphynes are porous, having a direct electronic bandgap[31] and tunable electronic behavior.[32]

Graphynes exhibit unique properties, including negative thermal expansion,[33] high Poisson's ratio,[33,34] negative linear compressibility,[34] and thermoelectric capabilities.[35] Computational investigations have extended to graphyne scrolls,[36] nanoribbons,[37] and nanotubes.[38] Although the acetylene chains in graphynes are substantially reactive, Solis et al.[36] showed that graphynes are thermally stable structures, at least up to 1000 K.

After multiple attempts to produce acetylenic oligomers,[39,40] Li et al.[41] achieved a breakthrough by synthesizing the most symmetric form of graphyne with $n = 2$, known as γ-graphdiyne. Subsequently, two groups reported the synthesis of $n = 4$ graphtetraynes 8−10 years later.[42,43] Remarkably, in 2022, three independent groups reported scalable syntheses of the most symmetric and densest form of $n = 1$ graphyne, the γ-graphyne.[44−46] These synthetic achievements are of significant importance. The possibility of large-quantity graphyne synthesis poses graphynes as a potential candidate to replace graphene in some applications. In fact, γ-graphyne has already found diverse applications, such as desalinators,[47] photocatalysts,[48] supercapacitors,[49] environmental remediation,[50] and sensors,[51] among others.[52] The synthesis of the densest form of graphyne opens up new possibilities for innovative applications.

In this work, we have used classical reactive molecular dynamics (MD) simulations to investigate the eC effects in monolayers of γ-graphyne. Using a previously defined Otto-like thermodynamic cycle,[23] our computational protocol provides adiabatic temperature changes and COP values for the cycle's cooling and heating phases. This investigation explores the role of the substrate, boundary conditions, and a specific regime of initial pre-elongation on the intensity and efficiency of the eC effect in γ-graphyne. By offering the first estimate for the COP of graphyne as solid refrigerants for both cooling and heating applications, this research fills a gap in the literature concerning this material.

2. METHODOLOGY

Fully atomistic MD simulations, using the adaptive intermolecular reactive empirical bond order (AIREBO) potential,[53,54] were carried out to investigate the effects of eC on γ-graphyne nanoribbons. Although thermal properties could be calculated from ab initio methods,[55] structure size and conditions for the investigation of the eC effect are better described with classical methods. The AIREBO potential is well-known for its effectiveness in reliably describing different carbon nanostructures.[56−58] The simulations were designed to determine the eC temperature changes and COP magnitudes. It should be noted that AIREBO has already been widely adopted for studying the structure, mechanical, and thermal properties of graphynes.[33,34,59,60]

The simulations were carried out using the Large-Scale Atomic/Molecular Massively Parallel Simulator (LAMMPS) package.[61] To characterize the eC effect, we performed simulations of the proposed Otto cycle,[23] determining temperature changes (ΔT) and energy quantities necessary for estimating the COP of graphyne nanoribbons. We have investigated the eC effect of nanoribbons cut along the zigzag and armchair directions. Figure 1 illustrates the structures, a qualitative diagram depicting the thermodynamic cycle, and the equilibrium states used to determine the eC effect in graphynes.

The hydrogen-passivated γ-graphyne nanoribbons considered in this study cut along the zigzag and armchair directions are depicted in Figures 1A and B, respectively. They exhibit dimensions of approximately 96.5 × 29.3 Å (zigzag) and 110.0 × 34.7 Å (armchair). The initial energy minimization was performed for all structures using the LAMMPS package conjugate gradient algorithms to obtain the minimum energy configuration. Energy and force convergence criteria during minimizations were set to 10^{-8} and 10^{-8} eV/Å, respectively,

https://doi.org/10.1021/acsami.4c03302
ACS Appl. Mater. Interfaces 2025, 17, 13074−13082

with convergence ensured following the protocols by Sihn et al.[62]

For the infinite structures (periodic boundary conditions), equilibrium at zero strain and initial operating temperature (T_0 = 300 K) was achieved through MD simulation lasting 1 ns. A time step of 0.5 fs and a fixed number of atoms (N), temperature (T_0), and pressure (P = 0) were maintained. Atom positions and the nanoribbon box size along the length direction were allowed to equilibrate.

For the finite structures, equilibrium at zero strain and initial operating temperature (T_0 = 300 K) was attained through a 60 ps of MD simulation. A time step of 0.5 fs, a Langevin thermostat at T_0, and the constraint of allowing only the atoms at the extremities (orange atoms in Figure 1) to move along the length direction of the nanoribbon were applied to equilibrate the positions of the atoms and the length of the structure.

These simulations were performed with the LAMMPS parameters PDAMP = 0.5 ps and TDAMP = 1 ps. Then, the equilibrium length, L_0, is taken from the average structure length values during the last 20 ps of the simulations. L_0 defines the zero strain state of the structures.

The thermodynamic cycle, shown in Figure 1C, has four paths through equilibrium states numbered 1−4. State number 1 represents the structure at the initial deformation configuration (which may not always be zero, as explained ahead) and the operating temperature, T_0. Two paths are isostrain (4 → 1 and 2 → 3), and two are adiabatic (1 → 2 and 3 → 4). Isostrain paths involve attaching a thermal bath to the system at the operating temperature, T_0 = 300 K. The two adiabatic routes increase and decrease the tensile strain between ε_i and ε_i + 0.1.

The simulation protocols for the thermodynamic cycles are as follows: For isostrain paths, we perform simulations for a total of 60 ps with a time step of 0.5 fs. We maintain the strain (or fixed structure size) and apply a Langevin thermostat with TDAMP = 1 ps. For adiabatic tensile and tensile release strain paths, we start the simulations with a T_0 = 300 K Boltzmann distribution of velocities to ensure that the initial temperature aligns with the operating one. Subsequently, we apply a strain rate of 0.1% ps^{-1} for 100 ps. These simulations proceed without a thermostat and with a time step of, at least, 0.05 fs. We set the final strain to be 10% above the initial strain. Recognizing the potential impact of the strain rate on the eC results, we present preliminary tests in Section S1 of the Supporting Information (SI) to assess the convergence of the COP results for different strain rates, providing further information.

The following combinations of conditions were considered for each γ-graphyne nanoribbon in this study:

(i) two pre-elongation regimes, i.e., two thermodynamic cycles with one starting from zero strain (ε_i = 0) and the other starting at a specific value (ε_i = ε_0);

(ii) two boundary conditions, i.e., the nanoribbons will be simulated with periodic boundary conditions (PBC) and finite length (FL);

(iii) two environmental conditions, i.e., suspended nanoribbons in space (SUS) and nanoribbons deposited on a substrate (SUBS).

Combinations of these conditions result in 16 groups of simulations (each pre-elongation regime for each boundary condition for each environment condition, or 2 × 2 × 2 = 16 different sets of conditions), hereafter referred to as "groups". Each group involves performing 10 simulations that satisfy the same (i), (ii), and (iii) conditions. However, each simulation starts from a statistically (microcanonically) different initial condition corresponding to the same macroscopic condition. This diversity is achieved by providing distinct initial velocity distributions among the system's atoms while maintaining the same T_0.

To determine the values of ε_0 for simulations under the second condition (i), we use the eC temperature changing profile during the expansion path of the thermodynamic cycles with ε_i = 0. Within each group, we obtain 10 different values of ε_{0j} and calculate the corresponding ε_0 for the group as the average over these 10 values. We derive each ε_{0j} by fitting a previously smooth-averaged T versus ε curve, corresponding to the expansion path of a single simulation within the group, to a second-degree polynomial with four parameters: $y = a(x + b)^2 + cx + d$. Section S2 in the SI provides an illustrative example of determining one ε_{0j}. In contrast, Section S3 of the SI displays typical examples of 10 microcanonically different but macroscopically equivalent temperature profiles during the adiabatic paths.

The substrate was simulated through an infinite artificial wall that interacts with the nanoribbons through a 12−6 Lennard-Jones function with ϵ = 0.002 844 eV, σ = 2.9 Å, and a cutoff of 10.0 Å. These parameters lead the equilibrium substrate−nanoribbons distance to be 3.4 Å.

Since classical MD simulations do not directly incorporate quantum effects on the heat capacity of the structures, and assuming that the heat exchanged with a thermal bath remains consistent regardless of whether we calculate the temperature change using classical or quantum methods, we utilize the following relationship to derive the actual temperature change, ΔT_{REAL}:

$$Q = C_{MD}\Delta T_{MD} = C_{REAL}\Delta T_{REAL} \quad (1)$$

Equation 1 is expressed as C_{MD} and ΔT_{MD} representing the heat capacity and eC temperature change of the structure obtained from MD simulations, respectively. Additionally, C_{REAL} signifies the real heat capacity of graphyne at the operating temperature, T_0. In the second equality, both sides of eq 1 can be divided by the sample mass, making it applicable for C to represent the specific heat in J/(g·K) instead of heat capacity. The value of C_{REAL} for graphyne was obtained from density functional theory (DFT) calculations carried out as follows.

Calculating constant-volume heat capacities for γ-graphyne nanoribbons involved using the Quantum Espresso (QE) code.[63] The QE-DFT calculations used a plane-wave basis set and pseudopotentials method. The interactions between electrons and atomic cores are described by expanding the wave function using plane-wave and norm-conserving pseudopotentials. Norm-conserving pseudopotentials, generated using the Troullier−Martins method[64] with the Perdew−Burke−Ernzerhof (PBE) functional, were used to account for both exchange energies and electronic exchange-correlation effects.[65,66]

We applied the Broyden−Fletcher−Goldfarb−Shanno (BFGS) scheme to optimize the crystal structure in our model sheets, as implemented in the QE code. We adopted high cutoff values, set at 70 Ry for wave functions and 700 Ry for charge density. Electronic self-consistency was achieved with a convergence criterion of 1.0 × 10^{-5} eV. Throughout

https://doi.org/10.1021/acsami.4c03302
ACS Appl. Mater. Interfaces 2025, 17, 13074−13082

Table 1. Real eC Temperature Changes (ΔT_{REAL} in K), Averaged over the 10 Statistically Different Simulations within Each Group of Conditions, for the Armchair (AC) And Zigzag (ZZ) Structures during the Expansion and Contraction Paths of the Thermodynamic Cycle[a]

	Finite-Length Conditions							
	suspended				substrate			
chirality	AC		ZZ		AC		ZZ	
initial strain	$\varepsilon_i = 0$	$\varepsilon_i = \varepsilon_0$	$\varepsilon_i = 0$	$\varepsilon_i = \varepsilon_0$	$\varepsilon_i = 0$	$\varepsilon_i = \varepsilon_0$	$\varepsilon_i = 0$	$\varepsilon_i = \varepsilon_0$
expansion	15.5	124.6	23.8	184.1	39.9	118.1	8.3	170.4
contraction	34.2	139.2	4.8	203.2	49.9	140.7	15.8	224.6
	Periodic Boundary Conditions							
	suspended				substrate			
chirality	AC		ZZ		AC		ZZ	
initial strain	$\varepsilon_i = 0$	$\varepsilon_i = \varepsilon_0$	$\varepsilon_i = 0$	$\varepsilon_i = \varepsilon_0$	$\varepsilon_i = 0$	$\varepsilon_i = \varepsilon_0$	$\varepsilon_i = 0$	$\varepsilon_i = \varepsilon_0$
expansion	11.3	81.2	42.9	154.6	1.72	83.3	60.3	153.8
contraction	21.0	87.3	33.9	162.8	1.91	88.1	52.8	166.0

[a]The terms "finite length", "periodic boundary conditions", "suspended", and "substrate" are defined in the Methodology section.

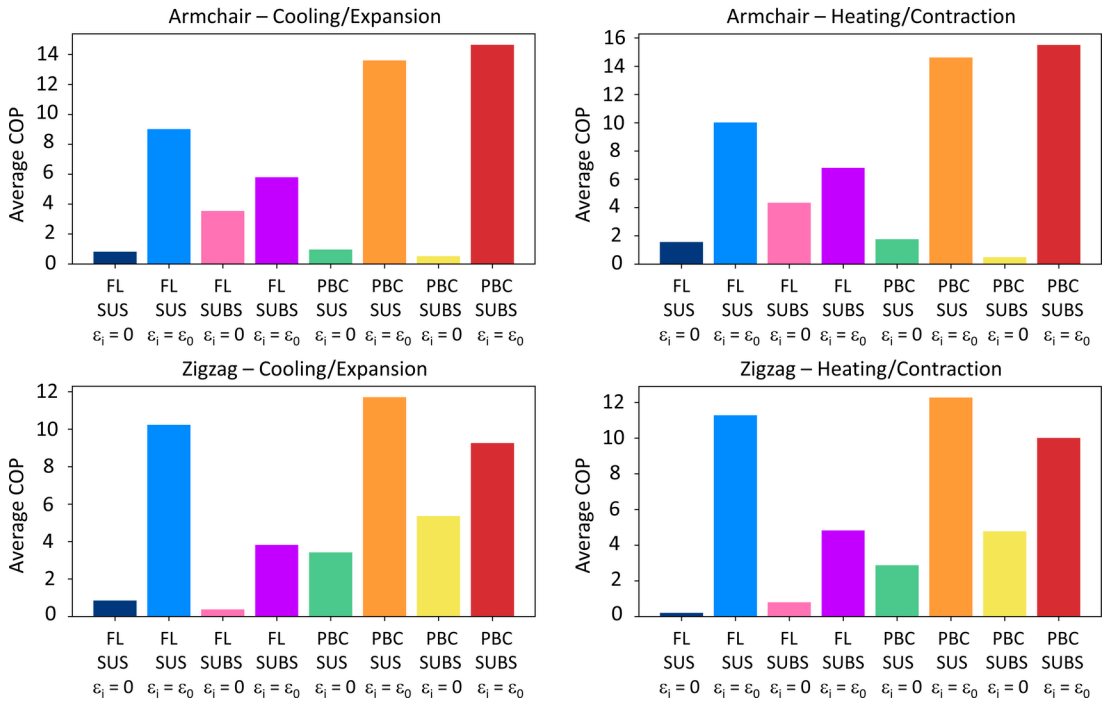

Figure 2. Average COP values across different simulated conditions for all structures during cooling/expansion and heating/contraction. The labels FL, PBC, SUS, and SUBS correspond to "finite length", "periodic boundary conditions", "suspended", and "substrate", respectively. For the definitions of these conditions, refer to the previous section. ε_i represents the strain of the initial state in the thermodynamic cycle.

lattice relaxation, the force on each atom was kept below 1.0×10^{-3} eV/Å.

We used the Phonopy package[67] alongside QE to address the lattice thermal properties of the studied materials. Phonons, serving as manifestations of vibrational modes within a crystal lattice, play a pivotal role in determining the thermal characteristics of materials. The seamless integration of Phonopy with QE allows precise computing of the force constants and provides essential insights for understanding phonon analyses and lattice thermal properties. For the computation of second- and third-order interatomic force constants, we applied the supercell finite-displacement approach with step sizes of 1.0×10^{-2} Å. Supercells containing 24 atoms were explicitly employed to calculate the second-order interatomic force constants. To ensure the accuracy and consistency of our results, we ran standard tests on parameters such as vacuum buffer layers, k-mesh points, energy cutoff values, and supercell sizes. Also, the phonon dispersion curve does not show imaginary frequencies, which supports structurally stable structures.

The COP corresponding to the cooling or heating device is given by

$$\mathrm{COP} = \frac{Q_C \text{ or } Q_H}{W} \tag{2}$$

In this expression, Q_C (or Q_H) and W denote the heat exchanged with the thermal bath after the cooling/expansion (or heating/contraction) paths and the total work per thermodynamic cycle, respectively. We can obtain Q_C or Q_H by multiplying the heat capacity by the corresponding ΔT since the work done by or on the system is null during the isostrain paths. No heat is exchanged during the adiabatic

https://doi.org/10.1021/acsami.4c03302
ACS Appl. Mater. Interfaces 2025, 17, 13074−13082

paths; then, the total work, W, done on the system during one thermodynamic cycle can be computed by summing the total internal energy differences of the system between thermodynamic states 2 and 1 ($W_{expansion} = E_2 - E_1$) and states 4 and 3 ($W_{contraction} = E_4 - E_3$), i.e.

$$W = W_{expansion} + W_{contraction} \quad (3)$$

3. RESULTS

In Table 1 and Figure 2, we present the averaged real eC temperature changes, ΔT_{REAL}, and the averaged COP for all structures simulated under different conditions. From now on, for temperature changes, we mean real temperature changes. Determining ΔT_{REAL} using eq 1 involves calculating the real and MD-specific heats of all structures. The real specific heat of γ-graphyne is considered as the one obtained from DFT calculations, denoted by c_{REAL} = 0.4383 J/g·K. The MD values of specific heat are detailed in Table S2 of the SI. Additionally, Section S4 of the SI provides two examples of a series of temperature equilibrations of the structures, ranging from 50 to 700 K, and their corresponding temperature and energy profiles necessary for determining the specific heat.

From Table 1, we can see that prestrained structures exhibit eC temperature changes at least 1 order of magnitude larger than initially unstrained structures, both during expansion and contraction. This trend is consistent with observations for the eC of prestrained rubber,[68] where an approximately 50% increase in the eC temperature change was observed. The most significant eC temperature changes in this study are observed for the finite-length suspended zigzag structure after the expansion path (ΔT_{REAL} = 184.1 K) and for the finite-length zigzag structure on the substrate after the contraction path (ΔT_{REAL} = 224.6 K).

Except for armchair structures under PBC (for both expansion and contraction paths) and finite-length zigzag structures (for expansion paths only), the enhancements in the eC temperature change by simply placing the structure on a substrate for unstrained ones can reach up to three times. Similar improvements in eC temperature change due to substrate adhesion were observed by Li et al.[69] for graphene, of the order of 30%. For prestrained structures, there is no significant difference in the eC temperature change between suspended and deposited on substrate γ-graphyne nanoribbons.

The temperature profiles presented in Figures S2−S5 reveal that during expansion (contraction), the eC temperature change corresponds to cooling (heating). This behavior is consistent with the observations made by Lisenkov et al.,[20] Cantuario and Fonseca,[23] Li et al.,[69] and Silva and Fonseca[24] for the eC of carbon nanotubes and graphene. However, this behavior is the opposite of that observed in rubber[68] and kirigami graphene,[25] where the eC temperature change is positive when stretched and negative when the strain is released.

The COP is as essential as the amount of eC temperature change, as it allows for comparing the efficiency of different refrigerators and heat pumps. While the best COP values of vapor-compression-based refrigerators are around 2.2,[70] our COP values ranged from as low as 1 up to 14. Instead of presenting the COP in a table, representing it in column bars is more effective for direct comparisons. In Figure 2, we show the COP values for all structures under all conditions considered in the present study. Like the eC temperature changes, prestrained structures exhibit much larger COP values than initially relaxed ones.

Figure 2 also indicates that, for unstressed armchair finite-length and zigzag PBC structures, depositing the γ-graphyne nanoribbon on a substrate enhances the elastocaloric efficiency compared to the suspended case, in agreement with the findings of Li et al.[69]

We would like to stress that, in contrast to Ni−Ti alloys or rubber, the elastocaloric effect in graphynes does not involve sudden structural changes. This behavior was observed for other carbon nanostructures,[20,23,24] and its origin remains unclear. To gain further insights into the significant increase in the efficiency of the elastocaloric-based refrigerator/heater with prestraining, we examined in detail the structures in their relaxed state. Lateral views of the equilibrated structures without prestrain are shown in Figure 3 for all boundary (ii) and environment (iii) conditions.

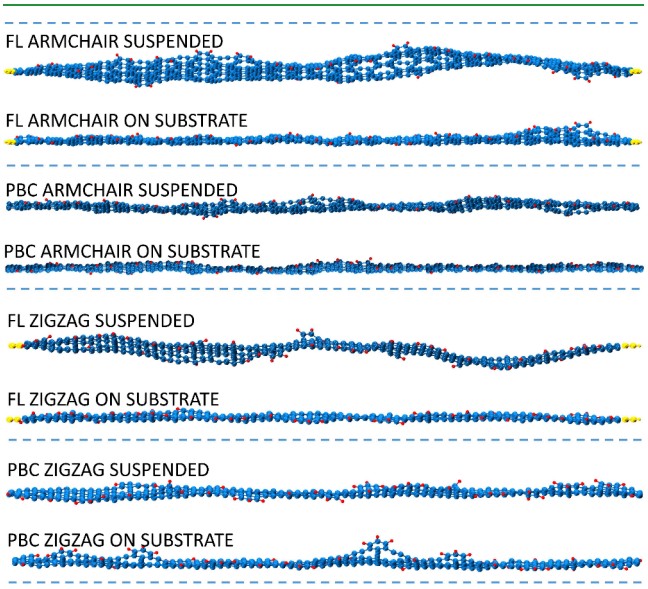

Figure 3. Lateral views of the armchair and zigzag structures on different boundary (ii) and environment (iii) conditions. FL and PBC denote "finite-length" and "periodic boundary conditions". Refer to the previous section for the meanings of these conditions. Dashed lines separate structures for each pair of environmental (iii) conditions. Movable carbon and hydrogen atoms and fixed carbon ones are shown in blue, red, and yellow colors, respectively.

Figure 3 illustrates that unstressed suspended structures exhibit a much more wavylike lateral form than those on the substrate. When a tensile strain is applied to the nanoribbon, its undulations become initially aligned. Then, its bonds start to be strained. We conjecture that this might be related to the increase and subsequent decrease of the eC temperature profile during both expansion and compression in unstrained structures. See the examples in Figures S2 and S4.

The straining of initially unstrained γ-graphyne nanoribbons during the expansion path can be divided into two phases. The first phase involves two effects: alignment of the nanoribbon chains with the direction of strain and some increase in carbon−carbon bond length values. The second phase comprises only bond length increase but at a slightly more significant rate. Only the second phase occurs when beginning the thermodynamic cycle from a prestrained structure. For this case, the eC temperature change exhibits a monotonically

https://doi.org/10.1021/acsami.4c03302
ACS Appl. Mater. Interfaces 2025, 17, 13074−13082

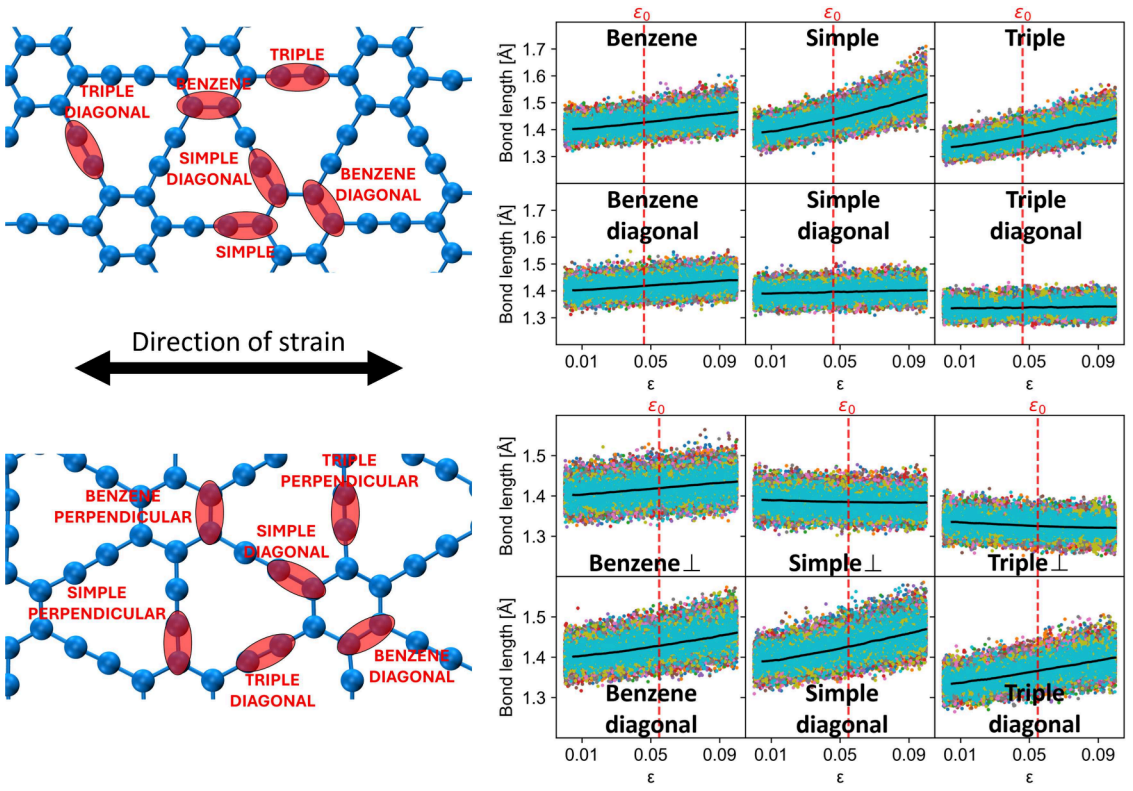

Figure 4. Evolution of the bond length values of six different carbon−carbon bonds in unstrained armchair (top) and zigzag (bottom) suspended structures. The highlighted sections of the armchair and zigzag structures on the left indicate these six bonds. Each type of bond length was measured in 30 different regions along the structure, plotting the strain values at intervals of 5×10^{-5}. Each dot color corresponds to one of these regions. The black curves represent the average smooth-average curves corresponding to the bond length values in one region. The symbol ⊥ denotes "perpendicular". Vertical dashed lines mark the corresponding value of ε_0 ($\varepsilon_0 = 0.046$ for armchair and $\varepsilon_0 = 0.055$ for zigzag nanoribbons). The green shades show the range of fluctuations in each measure.

decreasing (increasing) behavior when subjected to tensile strain (tensile strain release), as shown in the examples given in Figures S3 and S5.

Finally, to offer quantitative support for the above conjecture, we analyzed the evolution of the length of various carbon−carbon bonds in unstrained armchair and zigzag suspended structures during the expansion path. The results are presented in Figure 4.

The carbon−carbon bonds primarily bearing tension in the armchair structure are aligned directly with the strain direction. The diagonal carbon−carbon bonds are the ones that endure most of the tension in the zigzag structure. The most significant bond length increase occurs in the acetylenic simple bond aligned with the strain direction in armchair structures and benzene and acetylenic simple diagonal bonds in zigzag ones.

Upon inspecting the graphs for unstrained armchair structures, it becomes apparent that for $\varepsilon > \varepsilon_0$, the slope of the simple bond length versus ε curve is slightly higher than that for $\varepsilon < \varepsilon_0$. This difference is not visually discernible in the case of the primary bonds in zigzag structures. To provide more quantitative evidence for this observation, we performed a linear fitting to the average curves of carbon−carbon bond length versus ε in two regions: $\varepsilon < \varepsilon_0$ and $\varepsilon > \varepsilon_0$. The results are presented in Table 2.

The results in Table 2 demonstrate a significant change in the rate of bond length variation with strain at ε_0 for the specific bonds that experience most of the overall structural strain. The difference in the rate is noticeable in the first decimal point for these primary carbon−carbon bonds (highlighted in bold in Table 2). Meanwhile, there is virtually no change in the rate of bond length variation for the diagonal bonds in armchair structures and the perpendicular (⊥) bonds in zigzag ones. The negative rate of variation of the perpendicular bonds with strain indicates the positive Poisson's ratio nature of the structure. Therefore, Table 2 results suggest

Table 2. Change Rates of the Bond Length Values of the Different Carbon−Carbon Bonds with ε (in Å) for the Bonds Shown in Figure 4, for Armchair (AC) and Zigzag (ZZ) Structures Considered in Figure 4[a]

structure and type of bond	bond length rates for $\varepsilon < \varepsilon_0$	bond length rates for $\varepsilon > \varepsilon_0$
AC benzene	**0.634**	**0.716**
AC simple	**1.223**	**1.756**
AC triple	**1.033**	**1.225**
AC benzene diagonal	0.421	0.415
AC simple diagonal	0.145	0.144
AC triple diagonal	0.055	0.085
ZZ benzene diagonal	**0.557**	**0.721**
ZZ simple diagonal	**0.772**	**0.963**
ZZ triple diagonal	**0.657**	**0.731**
ZZ benzene ⊥	0.357	0.356
ZZ simple ⊥	−0.106	−0.019
ZZ triple ⊥	−0.204	−0.087

[a]The results for the bonds that experience the largest strains are highlighted in **bold**. The types of the bonds are shown in Figure 4. The symbol ⊥ means "perpendicular".

https://doi.org/10.1021/acsami.4c03302
ACS Appl. Mater. Interfaces 2025, 17, 13074−13082

a strong correlation between the rate of carbon−carbon bond length variation and the sign of variation of the eC temperature changes.

4. CONCLUSIONS

In summary, we explored the eC properties of nanoribbons of γ-graphyne along armchair and zigzag directions under various conditions. We simulated thermodynamic cycles, incorporating isostrain and adiabatic paths, for γ-graphyne structures with different configurations, such as finite length, periodic boundary conditions, suspended, and deposited on a substrate. As the main focus on the work is to evaluate the elastocaloric effect in graphynes, and pristine graphynes are thermally very stable, so only nonreactive substrates were considered in this work. Our findings indicated that placing the nanoribbon on a substrate for initially unstrained structures enhances its eC temperature change and COP values. However, the most substantial improvements in eC temperature change and COP were observed for initially prestrained structures, irrespective of whether they were being deposited on a substrate or suspended, finite, or with PBC. Additionally, we carried out a detailed analysis of the evolution of carbon−carbon bond lengths, revealing a correlation between the change in the rate of bond length variation with strain and the sign change in eC temperature changes.

■ ASSOCIATED CONTENT

Supporting Information

The Supporting Information is available free of charge at https://pubs.acs.org/doi/10.1021/acsami.4c03302.

Strain rate tests; initial strain determination (to determine the prestrained structures); typical curves for the MD values of eC temperature change; and the MD results for the calculation of the MD specific heat of graphyne (PDF)

■ AUTHOR INFORMATION

Corresponding Author

Alexandre F. Fonseca − *Universidade Estadual de Campinas, Instituto de Física Gleb Wataghin, Departamento de Física Aplicada, Campinas, São Paulo 13083-859, Brazil; Department of Mechanical and Civil Engineering, California Institute of Technology, Pasadena, California 91125, United States;* orcid.org/0000-0001-8413-9744; Email: afonseca@ifi.unicamp.br

Authors

Guilherme B. Kanegae − *Universidade Estadual de Campinas, Instituto de Física Gleb Wataghin, Departamento de Física Aplicada, Campinas, São Paulo 13083-859, Brazil;* orcid.org/0000-0001-7200-5482

Marcelo L. Pereira Junior − *University of Brasília, Faculty of Technology, Department of Electrical Engineering, Brasília 70910-900, Brazil;* orcid.org/0000-0001-9058-510X

Douglas S. Galvão − *Universidade Estadual de Campinas, Instituto de Física Gleb Wataghin, Departamento de Física Aplicada, Campinas, São Paulo 13083-859, Brazil;* orcid.org/0000-0003-0145-8358

Luiz A. Ribeiro Junior − *University of Brasília, Institute of Physics and Computational Materials Laboratory, LCCMat, Brasília 70910-900, Brazil;* orcid.org/0000-0001-7468-2946

Complete contact information is available at: https://pubs.acs.org/10.1021/acsami.4c03302

Notes

The authors declare no competing financial interest.

■ ACKNOWLEDGMENTS

This work received partial support from Brazilian agencies CAPES, CNPq, FAPESP, and FAPDF. M.L.P.J. acknowledges the financial support from FAP-DF grant 00193-00001807/2023-16. L.A.R.J. acknowledges CAPES for partially financing this study—Finance Code 88887.691997/2022-00. CENAPAD-SP (Centro Nacional de Alto Desempenho em São Paul Universidade Estadual de Campinas-UNICAMP) provided computational support for L.A.R.J., M.L.P.J., A.F.F., and G.B.K. (proj634, proj960, and proj861). L.A.R.J. acknowledges the financial support from Brazilian Research Council FAP-DF grant 00193.00001808/2022-71, FAPDF-PRONEM grants 00193.00001247/2021-2, 00193-00001857/2023-95, 00193-00001782/2023-42, and CNPq grant 350176/2022-1. G.B.K. acknowledges support from the Coordenação de Aperfeiçoamento de Pessoal de Nível Superior-Brasil (CAPES)-Finance Code 001. A.F.F. is a fellow of the Brazilian Agency CNPq-Brazil (303284/2021-8) and acknowledges grants #2020/02044-9 and #2023/02651-0 from São Paulo Research Foundation (FAPESP). L.A.R.J. and M.L.P. also thank Núcleo de Computação de Alto Desempenho (NACAD) for computational facilities through the Lobo Carneiro Supercomputer. D.S.G. acknowledges support from the FAPESP/CEPID grant #2013/08293-7.

■ REFERENCES

(1) Glass, L.-M.; Newig, J. Governance for achieving the Sustainable Development Goals: How important are participation, policy coherence, reflexivity, adaptation and democratic institutions? *Earth System Governance* **2019**, *2*, 100031.

(2) Dong, Y.; Coleman, M.; Miller, S. A. Greenhouse Gas Emissions from Air Conditioning and Refrigeration Service Expansion in Developing Countries. *Annual Review of Environment and Resources* **2021**, *46*, 59−83.

(3) Payal; Pandey, P. Role of nanotechnology in electronics: A review of recent developments and patents. *Recent Patents Nanotechnol.* **2022**, *16*, 45−66.

(4) El-Kady, M. M.; Ansari, I.; Arora, C.; Rai, N.; Soni, S.; Verma, D. K.; Singh, P.; Mahmoud, A. E. D. Nanomaterials: A comprehensive review of applications, toxicity, impact, and fate to environment. *J. Mol. Liq.* **2023**, *370*, 121046.

(5) Pokrajac, L.; Abbas, A.; Chrzanowski, W.; Dias, G. M.; Eggleton, B. J.; Maguire, S.; Maine, E.; Malloy, T.; Nathwani, J.; Nazar, L.; Sips, A.; Sone, J.; van den Berg, A.; Weiss, P. S.; Mitra, S. Nanotechnology for a Sustainable Future: Addressing Global Challenges with the International Network4Sustainable Nanotechnology. *ACS Nano* **2021**, *15*, 18608−18623.

(6) Debnath, S.; Reddy, M. M.; Yi, Q. S. Environmental friendly cutting fluids and cooling techniques in machining: a review. *Journal of cleaner production* **2014**, *83*, 33−47.

(7) Mañosa, L.; Planes, A.; Acet, M. Advanced materials for solid-state refrigeration. *J. Mater. Chem. A* **2013**, *1*, 4925−4936.

(8) Moya, X.; Kar-Narayan, S.; Mathur, N. D. Caloric materials near ferroic phase transitions. *Nat. Mater.* **2014**, *13*, 439−450.

(9) Chauhan, A.; Patel, S.; Vaish, R.; Bowen, C. R. A review and analysis of the elasto-caloric effect for solid-state refrigeration devices: Challenges and opportunities. *MRS Energy & Sustainability* **2015**, *2*, No. E16.

(10) Cazorla, C. Novel mechanocaloric materials for solid-state cooling applications. *Appl. Physics Rev.* **2019**, *6*, 041316.

(11) Miliante, C. M.; Christmann, A. M.; Usuda, E. O.; Imamura, W.; Paixão, L. S.; Carvalho, A. M. G.; Muniz, A. R. Unveiling the Origin of the Giant Barocaloric Effect in Natural Rubber. *Macromolecules* **2020**, *53*, 2606−2615.
(12) Escorihuela-Sayalero, C.; Pardo, L. C.; Romanini, M.; Obrecht, N.; Loehlé, S.; Lloveras, P.; Tamarit, J.-L.; Cazorla, C. Prediction and understanding of barocaloric effects in orientationally disordered materials from molecular dynamics simulations. *npj Comput. Mater.* **2024**, *10*, 13.
(13) Xie, Z.; Sebald, G.; Guyomar, D. Temperature dependence of the elastocaloric effect in natural rubber. *Phys. Lett. A* **2017**, *381*, 2112−2116.
(14) Wang, R.; Fang, S.; Xiao, Y.; Gao, E.; Jiang, N.; Li, Y.; Mou, L.; Shen, Y.; Zhao, W.; Li, S.; Fonseca, A. F.; Galvão, D. S.; Chen, M.; He, W.; Yu, K.; Lu, H.; Wang, X.; Qian, D.; Aliev, A. E.; Li, N.; Haines, C. S.; Liu, Z.; Mu, J.; Wang, Z.; Yin, S.; Lima, M. D.; An, B.; Zhou, X.; Liu, Z.; Baughman, R. H. Torsional refrigeration by twisted, coiled, and supercoiled fibers. *Science* **2019**, *366*, 216−221.
(15) Cui, J.; Wu, Y.; Muehlbauer, J.; Hwang, Y.; Radermacher, R.; Fackler, S.; Wuttig, M.; Takeuchi, I. Demonstration of high efficiency elastocaloric cooling with large ΔT using NiTi wires. *Appl. Phys. Lett.* **2012**, *101*, 073904.
(16) Mañosa, L.; Jarque-Farnos, S.; Vives, E.; Planes, A. Large temperature span and giant refrigerant capacity in elastocaloric Cu-Zn-Al shape memory alloys. *Appl. Phys. Lett.* **2013**, *103*, 211904.
(17) Qian, S.; Geng, Y.; Wang, Y.; Ling, J.; Hwang, Y.; Radermacher, R.; Takeuchi, I.; Cui, J. A review of elastocaloric cooling: Materials, cycles and system integrations. *International journal of refrigeration* **2016**, *64*, 1−19.
(18) Bruederlin, F.; Bumke, L.; Chluba, C.; Ossmer, H.; Quandt, E.; Kohl, M. Elastocaloric cooling on the miniature scale: a review on materials and device engineering. *Energy Technology* **2018**, *6*, 1588−1604.
(19) Imran, M.; Zhang, X. Reduced dimensions elastocaloric materials: A route towards miniaturized refrigeration. *Materials & Design* **2021**, *206*, 109784.
(20) Lisenkov, S.; Herchig, R.; Patel, S.; Vaish, R.; Cuozzo, J.; Ponomareva, I. Elastocaloric effect in carbon nanotubes and graphene. *Nano Lett.* **2016**, *16*, 7008−7012.
(21) Zhang, J. Elastocaloric effect on the piezoelectric potential of boron nitride nanotubes. *J. Phys. D: Appl. Phys.* **2017**, *50*, 415308.
(22) Patel, S.; Kumar, M. Elastocaloric effect in zinc oxide nanowire. *Functional Materials Letters* **2021**, *14*, 2150021.
(23) Cantuario, T. E.; Fonseca, A. F. High performance of carbon nanotube refrigerators. *Ann. Phys.* **2019**, *531*, 1800502.
(24) Silva, T. N. Y.; Fonseca, A. F. High performance of carbon nanotube elastocaloric refrigerators over a large temperature span. *Phys. Rev. B* **2022**, *106*, 165413.
(25) Ribeiro Junior, L. A.; Pereira Junior, M. L.; Fonseca, A. F. Elastocaloric effect in graphene kirigami. *Nano Lett.* **2023**, *23*, 8801−8807.
(26) Zhao, Z.; Guo, W.; Zhang, Z. Room-Temperature Colossal Elastocaloric Effects in Three-Dimensional Graphene Architectures: An Atomistic Study. *Adv. Funct. Mater.* **2022**, *32*, 2203866.
(27) Cai, J.; Yang, B.; Akbarzadeh, A. Origami Metamaterials Enable Low-Stress-Driven Giant Elastocaloric Effect. *ACS Nano* **2024**, *18*, 894−908.
(28) Baughman, R.; Eckhardt, H.; Kertesz, M. Structure-property predictions for new planar forms of carbon: Layered phases containing sp 2 and sp atoms. *J. Chem. Phys.* **1987**, *87*, 6687−6699.
(29) Chen, J.; Xi, J.; Wang, D.; Shuai, Z. Carrier Mobility in Graphyne Should Be Even Larger than That in Graphene: A Theoretical Prediction. *J. Phys. Chem. Lett.* **2013**, *4*, 1443−1448.
(30) Cranford, S. W.; Buehler, M. J. Mechanical properties of graphyne. *Carbon* **2011**, *49*, 4111−4121.
(31) Malko, D.; Neiss, C.; Viñes, F.; Görling, A. Competition for Graphene: Graphynes with Direction-Dependent Dirac Cones. *Phys. Rev. Lett.* **2012**, *108*, 086804.
(32) Padilha, J. E.; Fazzio, A.; da Silva, A. J. R. Directional Control of the Electronic and Transport Properties of Graphynes. *J. Phys. Chem. C* **2014**, *118*, 18793−18798.
(33) Hernandez, S. A.; Fonseca, A. F. Anisotropic elastic modulus, high Poisson's ratio and negative thermal expansion of graphynes and graphdiynes. *Diamond Relat. Mater.* **2017**, *77*, 57−64.
(34) Kanegae, G. B.; Fonseca, A. F. Effective acetylene length dependence of the elastic properties of different kinds of graphynes. *Carbon Trends* **2022**, *7*, 100152.
(35) Sevinçli, H.; Sevik, C. Electronic, phononic, and thermoelectric properties of graphyne sheets. *Appl. Phys. Lett.* **2014**, *105*, 223108.
(36) Solis, D. A.; D. Borges, D.; Woellner, C. F.; Galvao, D. S. Structural and thermal stability of graphyne and graphdiyne nanoscroll structures. *ACS Appl. Mater. Interfaces* **2019**, *11*, 2670−2676.
(37) Liu, Q.; Wang, X.; Yu, J.; Wang, J. Graphyne and graphdiyne nanoribbons: from their structures and properties to potential applications. *Phys. Chem. Chem. Phys.* **2024**, *26*, 1541−1563.
(38) Coluci, V.; Braga, S.; Legoas, S.; Galvao, D.; Baughman, R. Families of carbon nanotubes: Graphyne-based nanotubes. *Phys. Rev. B* **2003**, *68*, 035430.
(39) Kehoe, J. M.; Kiley, J. H.; English, J. J.; Johnson, C. A.; Petersen, R. C.; Haley, M. M. Carbon networks based on dehydrobenzoannulenes. 3. synthesis of graphyne substructures. *Org. Lett.* **2000**, *2*, 969−972.
(40) Haley, M. M. Synthesis and properties of annulenic subunits of graphyne and graphdiyne nanoarchitectures. *Pure Appl. Chem.* **2008**, *80*, 519−532.
(41) Li, G.; Li, Y.; Liu, H.; Guo, Y.; Li, Y.; Zhu, D. Architecture of graphdiyne nanoscale films. *Chem. Commun.* **2010**, *46*, 3256−3258.
(42) Gao, J.; Li, J.; Chen, Y.; Zuo, Z.; Li, Y.; Liu, H.; Li, Y. Architecture and properties of a novel two-dimensional carbon material-graphtetrayne. *Nano Energy* **2018**, *43*, 192−199.
(43) Pan, Q.; Chen, S.; Wu, C.; Shao, F.; Sun, J.; Sun, L.; Zhang, Z.; Man, Y.; Li, Z.; He, L.; Zhao, Y. Direct Synthesis of Crystalline Graphtetrayne—A New Graphyne Allotrope. *CCS Chemistry* **2021**, *3*, 1368−1375.
(44) Hu, Y.; Wu, C.; Pan, Q.; Jin, Y.; Lyu, R.; Martinez, V.; Huang, S.; Wu, J.; Wayment, L. J.; Clark, N. A.; et al. Synthesis of γ-graphyne using dynamic covalent chemistry. *Nat. Synth.* **2022**, *1*, 449−454.
(45) Desyatkin, V. G.; Martin, W. B.; Aliev, A. E.; Chapman, N. E.; Fonseca, A. F.; Galvão, D. S.; Miller, E. R.; Stone, K. H.; Wang, Z.; Zakhidov, D.; et al. Scalable synthesis and characterization of multilayer γ-graphyne, new carbon crystals with a small direct band gap. *J. Am. Chem. Soc.* **2022**, *144*, 17999−18008.
(46) Barua, M.; Saraswat, A.; Rao, C. A novel method for synthesis of γ-graphyne and their charge transfer properties. *Carbon* **2022**, *200*, 247−252.
(47) Mehrdad, M.; Moosavi, A. An efficient graphyne membrane for water desalination. *Polymer* **2019**, *175*, 310−319.
(48) Lin, Y.; Liu, H.; Yang, C.; Wu, X.; Du, C.; Jiang, L.; Zhong, Y. Gama-graphyne as photogenerated electrons transfer layer enhances photocatalytic performance of silver phosphate. *Applied Catalysis B: Environmental* **2020**, *264*, 118479.
(49) Chen, X.; Xu, W.; Song, B.; He, P. First-principles study of stability, electronic structure and quantum capacitance of B-, N-and O-doped graphynes as supercapacitor electrodes. *J. Phys.: Condens. Matter* **2020**, *32*, 215501.
(50) Majidi, S.; Erfan-Niya, H.; Azamat, J.; Cruz-Chú, E. R.; Walther, J. H. Efficient removal of heavy metals from aqueous solutions through functionalized γ-graphyne-1 membranes under external uniform electric fields: insights from molecular dynamics simulations. *J. Phys. Chem. B* **2021**, *125*, 12254−12263.
(51) Nikmanesh, S.; Safaiee, R.; Sheikhi, M. H. A novel high-performance methane sensor based on Ti-Decorated 2D γ-graphyne: A dispersion-corrected DFT insight. *Mater. Chem. Phys.* **2021**, *257*, 123808.
(52) Li, J.; Han, Y. Artificial carbon allotrope γ-graphyne: Synthesis, properties, and applications. *Giant* **2023**, *13*, 100140.

(53) Brenner, D. W.; Shenderova, O. A.; Harrison, J. A.; Stuart, S. J.; Ni, B.; Sinnott, S. B. A second-generation reactive empirical bond order (REBO) potential energy expression for hydrocarbons. *J. Phys.: Condens. Matter* **2002**, *14*, 783.
(54) Stuart, S. J.; Tutein, A. B.; Harrison, J. A. A reactive potential for hydrocarbons with intermolecular interactions. *J. Chem. Phys.* **2000**, *112*, 6472−6486.
(55) Sfuncia, G.; Nicotra, G.; Giannazzo, F.; Pécz, B.; Gueorguiev, G. K.; Kakanakova-Georgieva, A. 2D graphitic-like gallium nitride and other structural selectivity in confinement at the graphene/SiC interface. *CrystEngComm* **2023**, *25*, 5810−5817.
(56) Grantab, R.; Shenoy, V. B.; Ruoff, R. S. Anomalous Strength Characteristics of Tilt Grain Boundaries in Graphene. *Science* **2010**, *330*, 946−948.
(57) Muniz, A. R.; Fonseca, A. F. Carbon-Based Nanostructures Derived from Bilayer Graphene with Zero Thermal Expansion Behavior. *J. Phys. Chem. C* **2015**, *119*, 17458−17465.
(58) Chen, M.; Muniz, A. R.; Maroudas, D. Formation and Mechanical Behavior of Nanocomposite Superstructures from Interlayer Bonding in Twisted Bilayer Graphene. *ACS Appl. Mater. Interfaces* **2018**, *10*, 28898−28908.
(59) Zhang, Y. Y.; Pei, Q. X.; Wang, C. M. Mechanical properties of graphynes under tension: A molecular dynamics study. *Appl. Phys. Lett.* **2012**, *101*, 081909.
(60) Ma, S.; Zhang, M.; Sun, L.; Zhang, K. High-temperature behavior of monolayer graphyne and graphdiyne. *Carbon* **2016**, *99*, 547−555.
(61) Thompson, A. P.; Aktulga, H. M.; Berger, R.; Bolintineanu, D. S.; Brown, W. M.; Crozier, P. S.; in 't Veld, P. J.; Kohlmeyer, A.; Moore, S. G.; Nguyen, T. D.; Shan, R.; Stevens, M. J.; Tranchida, J.; Trott, C.; Plimpton, S. J. LAMMPS - a flexible simulation tool for particle-based materials modeling at the atomic, meso, and continuum scales. *Comput. Phys. Commun.* **2022**, *271*, 108171.
(62) Sihn, S.; Varshney, V.; Roy, A. K.; Farmer, B. L. Modeling for predicting strength of carbon nanostructures. *Carbon* **2015**, *95*, 181−189.
(63) Giannozzi, P.; Andreussi, O.; Brumme, T.; Bunau, O.; Nardelli, M. B.; Calandra, M.; Car, R.; Cavazzoni, C.; Ceresoli, D.; Cococcioni, M.; et al. Advanced capabilities for materials modelling with Quantum ESPRESSO. *J. Phys.: Condens. Matter* **2017**, *29*, 465901.
(64) Troullier, N.; Martins, J. L. Efficient pseudopotentials for plane-wave calculations. *Phys. Rev. B* **1991**, *43*, 1993.
(65) Perdew, J. P.; Burke, K.; Ernzerhof, M. Generalized gradient approximation made simple. *Physical review letters* **1996**, *77*, 3865.
(66) Ernzerhof, M.; Scuseria, G. E. Assessment of the Perdew−Burke−Ernzerhof exchange-correlation functional. *J. Chem. Phys.* **1999**, *110*, 5029−5036.
(67) Togo, A.; Tanaka, I. First principles phonon calculations in materials science. *Scripta Materialia* **2015**, *108*, 1−5.
(68) Xie, Z.; Sebald, G.; Guyomar, D. Elastocaloric effect dependence on pre-elongation in natural rubber. *Appl. Phys. Lett.* **2015**, *107*, 081905.
(69) Li, M.; Guo, Z.; Chang, T. Adhesion and stress-enhanced elastocaloric effect in graphene. *Science China Technological Sciences* **2020**, *63*, 297−302.
(70) Nandanwar, Y. N.; Walke, P. V.; Kalbande, V. P.; Mohan, M. Performance improvement of vapour compression refrigeration system using phase change material and thermoelectric generator. *International Journal of Thermofluids* **2023**, *18*, 100352.

https://doi.org/10.1021/acsami.4c03302
ACS Appl. Mater. Interfaces 2025, 17, 13074−13082